Nanoscale

PAPER

View Article Online
View Journal | View Issue

Cite this: *Nanoscale*, 2025, **17**, 1092

Gold nanoclusters $Au_{25}AcCys_{18}$ normalize intracellular ROS without increasing cytoplasmic alarmin acHMGB1 abundance in human microglia and neurons†

Issan Zhang, [a] Dusica Maysinger, *[a] Maja Beus, [a] Antonija Mravak, [b] Ziqi Yu,[c,d] Martina Perić Bakulić, [e,f] Patrick A. Dion,[d] Guy A. Rouleau,[d] Vlasta Bonačić-Koutecký, [f,g] Rodolphe Antoine [h] and Željka Sanader Maršić *[b,f]

This study focuses on the modulatory effects of gold nanoclusters with 25 gold atoms and 18 acetyl cysteines ($Au_{25}AcCys_{18}$) in human microglia, human iPSC-derived neurons and SH-SY5Y differentiated human neuronal cells. The combination of chemical, biological, and computational methods shows the well-retained viability of these human cells treated with $Au_{25}AcCys_{18}$, interactions between $Au_{25}AcCys_{18}$ and transcription factor TFEB (computational approach), interactions between TFEB and HMGB1 (proximity ligation assay and molecular modeling using AlphaFold), modulation of the abundance and location of acHMGB1 by $Au_{25}AcCys_{18}$ (immunocytochemistry), and the reduction of ROS in cells treated with $Au_{25}AcCys_{18}$ (CellROX live imaging). These novel findings in human neural cells, particularly neurons, encourage further studies in experimental animal models of neurological disorders and/or human organoids to exploit the unique structural and photophysical properties of gold nanoclusters and to better understand their ability to modulate molecular mechanisms in human cells.

Received 27th August 2024,
Accepted 16th November 2024

DOI: 10.1039/d4nr03512g

rsc.li/nanoscale

Introduction

The meteoric rise of nanomaterials for therapeutic purposes in the last few decades raised important questions at the cellular and subcellular levels. Gold nanoclusters (AuNCs) can be atomically precise, giving them molecule-like identities with highly predictable physicochemical properties.[1,2] Biological applications of AuNCs (*e.g.* photodynamic therapy and bioimaging) benefit from their size and ligand tunability.[2–4] Bare metal clusters are unstable in solution and need protection. The combination of metal nanoclusters with peptides or proteins brings together the unique optical, electronic, and catalytic properties of metal nanoclusters with the biological functions of biomolecules. Thiol-containing ligands such as glutathione,[5] mercaptoundecanoic acid,[6] and captopril[7] are used for specific functionalities and enhance the solubility of AuNCs in solvents. These ligands allow for precise control over the size, shape, and surface chemistry of AuNCs, facilitating their use in catalysis,[8] sensing,[9] and drug delivery.[10] Cysteine ligands notably stabilize AuNCs and facilitate interactions with cells. *N*-Acetyl-cysteine is water-soluble, endogenous and non-toxic at low concentrations. Au_{25} nanoclusters have been thoroughly characterized using high-resolution mass spectrometry. Their size strikes a balance, being small enough for bioactivity and avoiding the disruption of cellular proteins, yet large enough to avoid toxicity due to their excessive surface area, as seen in smaller nanoclusters.[11,12] $Au_{25}AcCys_{18}$ (Au_{25}: 25 gold atoms; AcCys: *N*-acetyl-cysteine) has a long lifetime and optical properties attractive for photosensitization.[3,13–15] Its early discovery, easy preparation, high stability, and exci-

[a]*Department of Pharmacology and Therapeutics, McGill University, 3655 Promenade Sir-William-Osler, H3G 1Y6 Montreal, Canada. E-mail: dusica.maysinger@mcgill.ca*
[b]*Faculty of Science, University of Split, Ruđera Boškovića 33, 21000 Split, Croatia. E-mail: zsm@pmfst.hr*
[c]*Division of Experimental Medicine, Faculty of Medicine, McGill University, Montreal, QC, Canada*
[d]*Montreal Neurological Institute, Department of Neurology and Neurosurgery, McGill University, Montreal, QC, Canada*
[e]*Faculty of Chemistry and Technology, University of Split, Ruđera Boškovića 35, 21000 Split, Croatia*
[f]*Center of Excellence for Science and Technology, Integration of Mediterranean Region (STIM), Faculty of Science, University of Split, Ruđera Boškovića 33, 21000 Split, Croatia*
[g]*Chemistry Department, Humboldt University of Berlin, Brook-Taylor-Strasse 2, 12489 Berlin, Germany*
[h]*Institut Lumière Matière, CNRS UMR 5306, Université Claude Bernard Lyon 1, Univ. Lyon, 69622 Villeurbanne Cedex, France*
† Electronic supplementary information (ESI) available. See DOI: https://doi.org/10.1039/d4nr03512g

tation in the ultraviolet-visible and near infrared regions (tunable photoluminescence and large Stokes shift) make it advantageous for biomedical applications.[16]

In the dynamic cellular environment, rapidly shifting oxidative states under physiological and pathological conditions can significantly affect $Au_{25}AcCys_{18}$ interactions. The brain maintains tight control of oxidative processes due to the sensitivity of neural cells and high energy demands.[17] Dysregulation and/or excessive stress associated with hypoxia or inflammation are hallmarks of many neurological disorders[18,19] and would affect the impact of $Au_{25}AcCys_{18}$ in cells. We have previously shown that human astrocytes respond to AuNCs in a size- and ligand-dependent manner at the level of organelles.[4] The present work focuses on microglia and neurons, which are particularly sensitive to reactive oxygen species (ROS) and redox imbalance. Activated microglia release ROS and soluble factors such as high mobility group box 1 (HMGB1), a multifaceted protein with emerging binding partners and functions under physiological and pathological conditions.[20,21]

We hypothesize that $Au_{25}AcCys_{18}$ can modulate cellular ROS under hypoxic and normoxic conditions. $Au_{25}AcCys_{18}$ could also modulate the localization of redox-responsive proteins such as HMGB1 and TFEB, as well as their protein–protein interactions, resulting in changes in lysosomal cathepsin B activity. The results show reduced ROS abundance and maintenance of low nuclear acetylated HMGB1 (acHMGB1) abundance both in human microglia and human iPSC-derived neurons. Collectively, the data suggest context-dependent biological effects of $Au_{25}AcCys_{18}$ as related to its nano-bio interactome.

Experimental

Gold nanocluster synthesis

$Au_{25}AcCys_{18}$ and $AcCys_{18}$ were provided by Dr Rodolphe Antoine from the Institut Lumière Matière, University of Lyon, France. The synthesis and characterization were described by Fakhouri *et al.*[3] A summary of their structures is provided in Fig. 1.

In silico modeling and analyses

The protein structures for HMGB1 (pdb: 2YRQ) and TFEB (pdb: AF_AFA0A024RCY3F1) were taken from the Protein Data Bank.[22] Interactions between TFEB and $Au_{25}AcCys_{18}$ or HMGB1 were predicted using AlphaFold.[23,24] The calculation of solvent accessible surface area (SASA) and molecular electrostatic potential (MEP) was performed in Jmol,[25] whereas the analysis of TFEB–{Cys_9} contact interactions was carried out in Chimerax.[26]

The density functional theory-optimized structure of $Au_{25}AcCys_{18}$ was taken from our previous study.[3] To calculate the interaction energy, we performed single point calculations using the Perdew–Burke–Ernzerhof functional[27,28] within Gaussian software. The split valence polarization (SVP) atomic orbital (AO) basis set[29] was used for gold and sulphur, and the 3-21G AO basis set[30,31] was used for all other atoms. For gold atoms, a relativistic effective core potential (19-e^- RECP) was employed.[32]

Solvent-Accessible Surface Area (SASA) represents the portion of a molecule that is available for contact with solvent (as opposed to the part that is buried inside). It is a key factor in understanding molecular interactions and behavior in biological environments. SASA is calculated by "rolling" a spherical probe (representing a solvent molecule) over the surface of the molecule we are investigating. The radius of this probe is usually set to the radius of a water molecule (~1.4 Å). The resulting surface area represents the part of the molecule that could interact with solvent molecules.

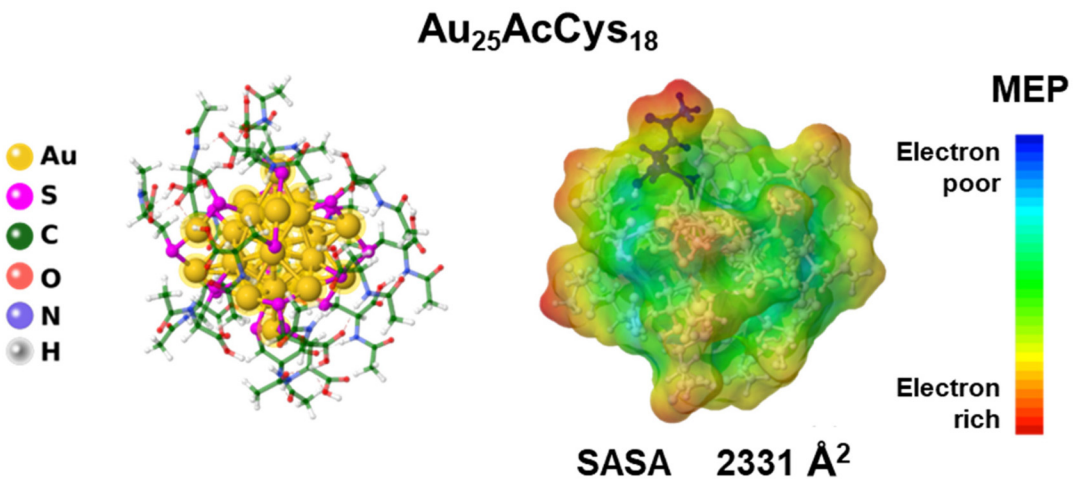

Fig. 1 Structure of the gold nanocluster $Au_{25}AcCys_{18}$ and atomic representation with a colour scheme (left). The icosahedral gold core and S–Au–S–Au–S staple motifs are highlighted, whereas acetyl cysteine (AcCys) ligands are presented as sticks.[3] Au = gold, S = sulfur, C = carbon, O = oxygen, N = nitrogen, and H = hydrogen. (Right) The solvent-accessible surface area (SASA) colored by molecular electrostatic potentials (MEPs) indicates the interacting surface of the nanocluster with the potential for electrostatic interactions.

Cell line culture

The human microglia (HMC3) and human neuroblastoma (SH-SY5Y) cell lines were originally obtained from the American Type Culture Collection. HMC3 cells were kept in Dulbecco's Modified Eagle's Medium (DMEM, Thermo Fisher Scientific) with 5% (v/v) fetal bovine serum (FBS, Wisent) and 1% (v/v) penicillin–streptomycin (Thermo Fisher Scientific). SH-SY5Y cells were maintained in F12/DMEM (Thermo Fisher Scientific) supplemented with 10% FBS and 1% penicillin–streptomycin. The cells were kept at 37 °C with 5% CO_2 and 95% relative humidity.

iPSC culture

Human iPSCs were generated from the lymphocytes of consenting individuals. The iPSC line SBP012 was reprogrammed as described previously.[33] iPSCs were cultured on a Matrigel (Corning) coated plate with mTeSR1 medium (STEMCELL Technologies) in a 100% humidity incubator at 37 °C and 5% CO_2.

Neuronal differentiation

Neural progenitor cells (NPCs) were induced using a STEMdiff™ SMADi Neural Induction kit (STEMCELL Technologies) according to the manufacturer's embryoid body (EB) protocol. On day 0, a single-cell suspension of iPSCs was generated using Gentle Cell Dissociation reagent and 10 000 cells per well were seeded in an ultra-low attachment 96-well plate (Corning) to form EBs. The cells were cultured in STEMdiff™ Neural Induction Medium with SMADi and 10 μM Y-27632. A partial medium change was performed daily from Day 1 to Day 4 using STEMdiff™ Neural Induction Medium with SMADi. On Day 5, EBs were collected using a 1 mL wide-bore serological pipette and a 40 μm strainer. EBs were then replated in a poly-L-ornithine hydrobromide (PLO) and laminin-coated 6-well plate (Corning). A full medium change was performed daily from day 6 to day 11. When the neural induction efficiency exceeds 75%, neural rosettes were manually selected on day 12 using the STEMdiff™ Neural Rosette Selection Reagent and replated onto a PLO/laminin-coated 6-well plate. Daily full medium changes were performed until the NPCs were ready for the first passage when cultures reached approximately 80–90% confluency. NPCs were maintained in STEMdiff™ Neural Progenitor Medium until ready for differentiation after two passages using Accutase (STEMCELL Technologies). For the final differentiation into forebrain neurons, NPCs were digested with Accutase and seeded onto PLO/laminin-coated glass coverslips (Mandel Scientific) with a STEMdiff™ Forebrain Neuron Differentiation Kit. Daily full medium changes were performed for 6 days before switching to the STEMdiff™ Forebrain Neuron Maturation Kit. Maturation media were changed twice a week until the neurons were ready for use.

Cell viability

Cells were seeded at 7000 cells (24 h treatment) or 5000 cells (72 h treatment) per well in 96-well plates (Sarstedt) and cultured overnight before treatment. For cell counting, the cells were incubated after treatment for 15 min with Hoechst 33342 (Millipore-Sigma, 10 μM) and imaged using a fluorescence microscope (Leica DMI4000B). Cell numbers were counted using the Cell Counter function in ImageJ (version 1.53t). For the MTT assay, the culture media were removed and the cells were incubated with 3-(4,5-dimethyl-2-thiazolyl)-2,5-diphenyl-2*H*-tetrazolium bromide (MTT, 0.5 mg mL^{-1}, Millipore-Sigma) dissolved in culture medium, for 30 min at 37 °C. The MTT media were removed and the cells were lysed in dimethyl sulfoxide (100 μL per well). The released formazan was measured colorimetrically at 595 nm using a microplate reader (Spark, Tecan).

Oxidative stress

Cells were seeded onto glass coverslips (12 mm diameter, Assistent) at 7000 cells per coverslip and cultured for 24 h. Hypoxic conditions (4 h) were achieved using a BioSpherix XvivoSystem model X3 Hypoxia Hood with a glovebox. Nitrogen gas was used to flush oxygen, and the conditions were set to 37 °C, 5% CO_2, and 1.0% O_2.

At the end of the treatment, the cells were incubated with CellROX Deep Red (5 μM, Thermo Fisher Scientific) and Hoechst 33342 (10 μM) for 30 min at 37 °C, in phenol- and serum-free DMEM (Thermo Fisher Scientific). The cells were washed in phenol- and serum-free DMEM before imaging with a fluorescence microscope. Fluorescence was analyzed in ImageJ.

Immunocytochemistry in cell lines

Cells were seeded onto glass coverslips at 7000 cells per coverslip and incubated for 24 h before treatment. The cells were washed twice with phosphate-buffered saline (PBS) and treated under serum-deprived conditions. Following treatment, the cells were fixed (4% (w/v) with paraformaldehyde, BDH, 10 min) and permeabilized (0.1% Triton X-100 (v/v), Millipore-Sigma, 10 min). The samples were incubated with primary antibodies (rabbit anti-acetylated HMGB1, 1/1000, MyBioSource, MBS9404216) overnight in 10% (v/v) goat serum (Thermo Fisher Scientific). The samples were washed thrice for 5 min with PBS and then incubated with secondary antibodies (goat anti-rabbit Alexa Fluor 647, 1/500, Thermo Fisher Scientific) for 1 h at room temperature, along with Hoechst 33342 (10 μM). The cells were washed thrice for 5 min with PBS and then mounted onto microscope slides using Aqua-Poly/Mount (Polysciences). Samples were imaged using a fluorescence microscope and fluorescence was analyzed in ImageJ.

Immunocytochemistry for iPSCs

iPSC-differentiated neurons were washed twice with PBS and fixed for 1 h with 5% (w/v) sucrose and 3.7% (w/v) formaldehyde in PBS at room temperature. Following fixation, neurons were permeabilized using the same buffer with 0.2% (v/v) Triton X-100 (2 min). The neurons were rinsed twice in PBS and incubated for 10 min in 50 mM NH4CI in PBS for 10 min, washed twice with PBS before blocking with 10% (v/v)

donkey serum (DS) in PBS for 20 min, and immunolabelled with primary antibodies diluted in 5% DS and 0.05% Triton X-100 in PBS overnight at 4 °C. The neurons were washed thrice with PBS for 5 min at room temperature and then incubated with secondary antibodies conjugated to Alexa 647 or Alexa 488 diluted in 5% DS and 0.05% Triton X-100 in PBS for 1 h. Neurons were washed thrice in PBS for 5 min. Hoechst 33342 (10 μM) was used to label nuclei for 10 min. Then the neurons were washed thrice with PBS and once in double distilled water, and were mounted with ProLong™ Diamond Antifade Mountant (Thermo Fisher Scientific). Images were acquired with a 63X lens on an SP8 confocal microscope (Leica Microsystems) and analyzed with ImageJ.

Proximity ligation assay

Cells were seeded onto glass coverslips for immunocytochemistry experiments. Following treatment, the cells were fixed (4% paraformaldehyde, 10 min) and permeabilized (0.1% Triton X-100, 10 min). The samples were blocked in Duolink blocking solution and incubated with primary antibodies overnight (rabbit anti-TFEB, 1/500, Sigma-Aldrich, SAB4503154; mouse anti-HMGB1, 1/500, Abcam, ab190377). The proximity ligation assay was then performed following the manufacturer's instructions for Duolink (Millipore-Sigma). In brief, the samples were washed twice in buffer A (5 minand then incubated with Plus and Minus probes for 1 h at 37 °C. The cells were washed twice and then incubated with ligase (30 min, 37 °C). The cells were washed again twice and then incubated with polymerase for signal amplification (100 min, 37 °C). For actin labelling, the cells were incubated with Alexa Fluor 488 Phalloidin (1/400, 20 min, Thermo Fisher Scientific). The samples were mounted onto glass slides with Duolink *in situ* mounting medium with DAPI and imaged using a fluorescence microscope.

Statistics

Statistical significance was calculated using one-way ANOVA followed by Dunnett's test. When the homogeneity of variance or sample size is not met, Welch's ANOVA followed by the Games-Howell test was performed. Experiments were performed independently at least three times. *p*-Values smaller than 0.05 were considered statistically significant.

Results

Structure and properties of $Au_{25}AcCys_{18}$

$Au_{25}AcCys_{18}$ exhibits unique structural properties that influence its behavior and functionality. The core consists of gold atoms arranged in an icosahedral Au_{13} kernel with a central Au atom, protected by six $Au_2(SR)_3$ staple motifs.[34,35] The ligands can significantly influence the AuNC properties. Both ligands and the nanocluster size play crucial roles in determining their activity and biodistribution *in vivo*. The choice of acetylcysteine (AcCys) as a protecting ligand for AuNCs was primarily for its biocompatibility and endogenous antioxidant properties.[36] AcCys at concentrations used in this study does not interfere with cellular functions, and its flexibility is influenced by H-bond networks. AcCys provides greater flexibility for AuNCs compared to larger ligands like glutathione,[3] owing to fewer H-bonds and allowing for structural flexibility and performance. The overall size of the nanocluster is approximately 2 nm, with a solvent-accessible surface area of 2331 $Å^2$, making it small enough for cellular uptake and interaction with biomolecules (Fig. 1).

Biological evaluation in human neural cells: viability and modulation of ROS

We first assessed the viability of human microglia and neurons in response to $Au_{25}AcCys_{18}$. These neural cell types play critical roles in the central nervous system under physiological and pathological conditions. Microglia are sensitive to foreign materials as they constantly survey the brain. Their response to nanostructures and other compounds sets the stage for therapeutic applications, as they directly and indirectly influence other neural cells. Neurons do not have the same ability as microglia to proliferate, and their loss is critical to brain health. We examined the potential toxicity of $Au_{25}AcCys_{18}$ by establishing time- and concentration-dependent effects on cell viability (cell count) after 24 h and 72 h (Fig. 2 and Fig. S1†). The results showed that $Au_{25}AcCys_{18}$ was well tolerated at the concentration used throughout this manuscript (1 μM) in both cell types.

Cellular redox is a fast-changing state that participates in cellular signalling. Altered redox as a result of changing energy expenditure or production influences the functionality of redox-sensitive proteins and pathways. A cellular response to $Au_{25}AcCys_{18}$ under conditions of oxidative stress was simulated chemically using the GSH inhibitor buthionine sulfoximine (BSO), as well as physically using a hypoxic chamber (Fig. 3). Depletion of antioxidant defences with BSO causes an increase in ROS, as detected with the fluorescent probe CellROX. Neuronal cells were more sensitive to hypoxia with GSH depletion, and $Au_{25}AcCys_{18}$ brought down ROS to near-control levels. This suggests a protective effect of $Au_{25}AcCys_{18}$ against excessive cellular ROS.

Modulation of HMGB1 localization

Microglial and neuronal cells are affected by pro-inflammagens such as lipopolysaccharides (LPSs), which activate a cascade of intracellular pathways culminating in the release of soluble factors such as HMGB1. HMGB1 is mostly concentrated in the nucleus, where it serves as a DNA-associated protein facilitating transcription. Inflammation and ROS induce post-translational modifications (*e.g.* acetylation) that relocate HMGB1 to the cytosol and extracellular space as a signalling protein, thus affecting neuron–neuron and neuron–glia interactions. Pharmacological manipulation using histone deacetylase inhibitors (ACY-1215, SAHA) increased the cellular level of acHMGB1 (Fig. 4 and 5). The concept is illustrated in Fig. 4a. We show the morphology of human microglia and neuron-like cells (differentiated SH-SY5Y), and the abundance

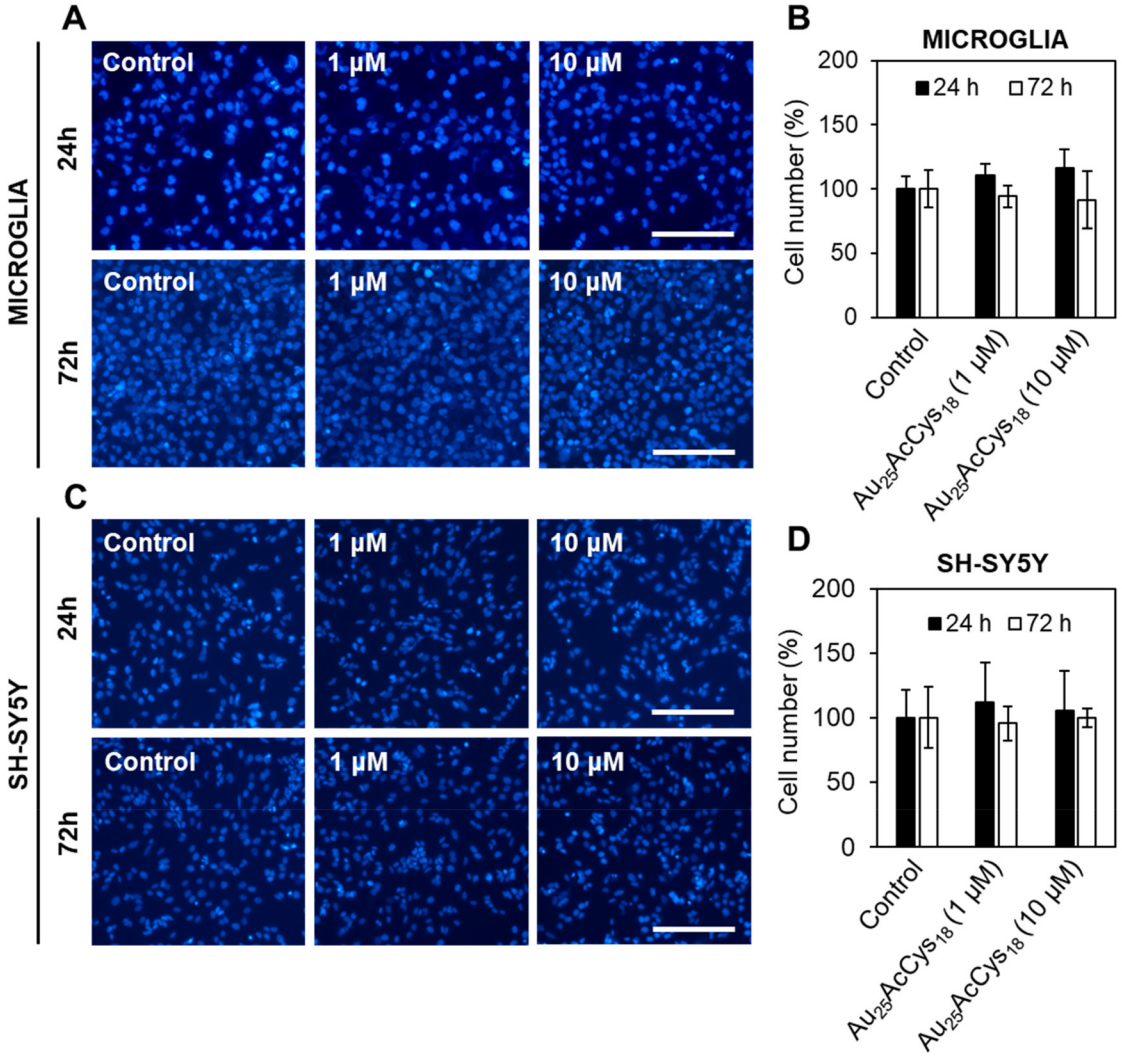

Fig. 2 $Au_{25}AcCys_{18}$ does not affect the viability of human microglia and differentiated SH-SY5Y neuronal cells after 24 h and 72 h. Fluorescence micrographs of (A) microglial and (C) differentiated neuronal cells treated with $Au_{25}AcCys_{18}$ for 24 h. Nuclei are labelled with Hoechst 33342 (blue). Average cell viability determined by cell nuclei counting normalized to the vehicle control ± SEM for (B) microglial and (D) differentiated neuronal cells. Scale bars = 40 μm.

of acHMGB1 under hypoxic and normoxic conditions (Fig. 4b and d). $Au_{25}AcCys_{18}$ itself maintains cytoplasmic acHMGB1 to a low, barely detectable level both in differentiated SH-SY5Y (Fig. 4d) and human neurons, comparable to untreated controls (Fig. 5). $Au_{25}AcCys_{18}$ does not significantly change the subcellular distribution of acHMGB1, as the effect of histone deacetylase inhibitors is very strong. Considering that HMGB1 translocates from the nucleus to the cytosol under cellular stress, we next investigated if cytosolic HMGB1 will associate with another stress-responsive transcription factor: TFEB.

Interaction with transcription factors TFEB and HMGB1

HMGB1 is a co-factor of numerous transcription factors. Its association with lysosomal compartments for cellular release suggests a potential interaction with the key lysosomal regulator TFEB.[37] Little is known about TFEB and HMGB1 interactions. We aimed to investigate the sites and characteristics of their interactions and compare them with the putative interactions of TFEB and $Au_{25}AcCys_{18}$. We employed AlphaFold (v.2.0), which uses an end-to-end deep neural network to predict protein structures from sequences, including protein complexes.[38] It has achieved unprecedented accuracy, significantly outperforming other methods in the latest Critical Assessment of Protein Structure Prediction (CASP14) round.[23] Fig. 6a presents the interaction sites for HMGB1 and $Au_{25}AcCys_{18}$ at the surface of TFEB, whereas Fig. S2† shows details that include TFEB amino acids interacting with HMGB1 *versus* $\{Cys_9\}$. Prediction of the TFEB and HMGB1 complex was done using their primary sequences, and AlphaFold provided their three-dimensional complex model, together with the predicted local distance difference test (pLDDT). The pLDDT is a per-residue confidence measure for

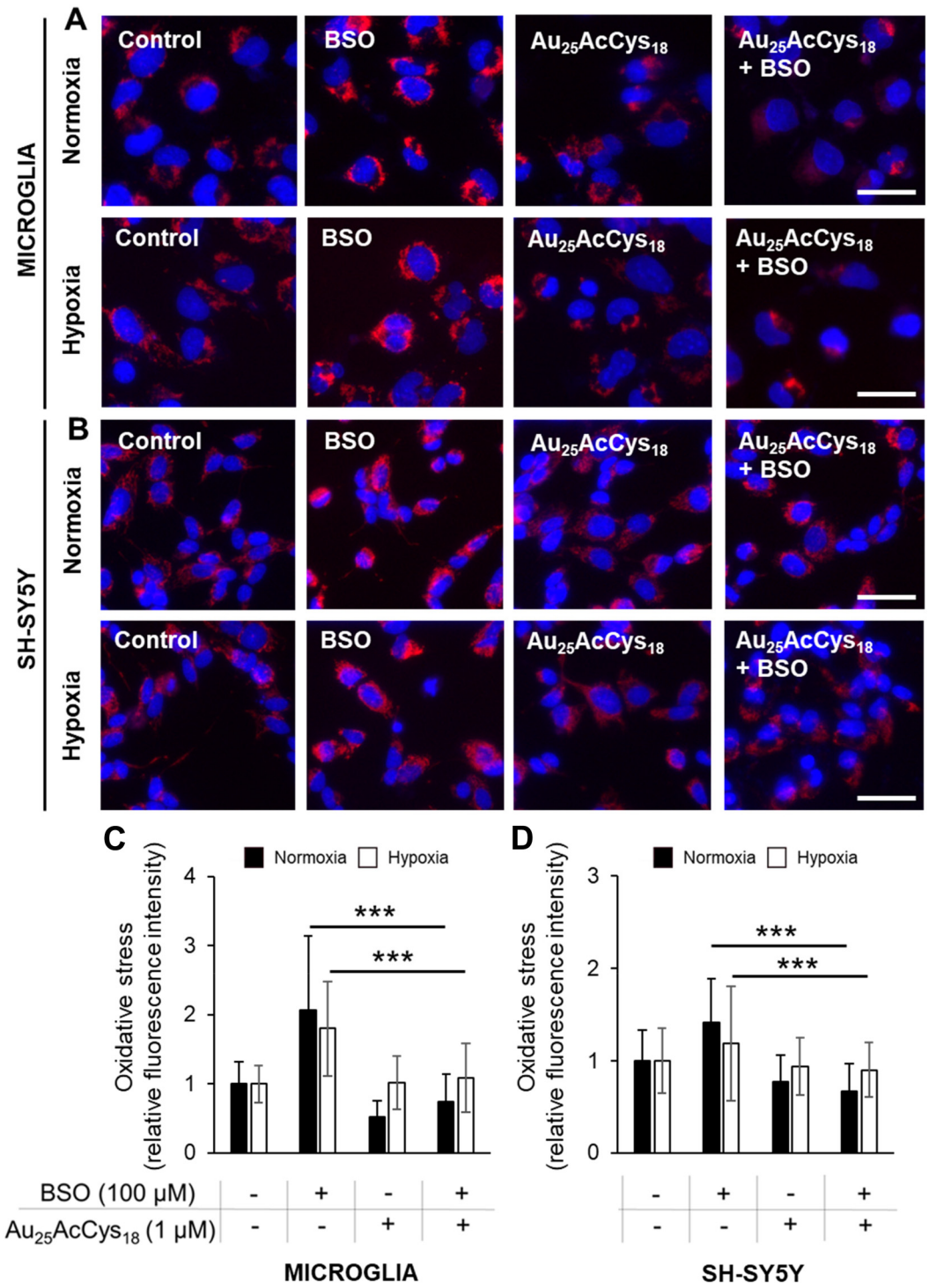

Fig. 3 $Au_{25}AcCys_{18}$ decreases the abundance of reactive oxygen species in human microglia and differentiated SH-SY5Y neuronal cells under normoxic and hypoxic conditions. Fluorescence micrographs of (A) microglial and (B) differentiated SH-SY5Y neuronal cells treated with L-buthionine sulfoximine (BSO; 100 μM) and $Au_{25}AcCys_{18}$ (1 μM) in serum-deprived media for 24 h under normoxic conditions and for 4 h under hypoxic conditions (1% O_2). Oxidative stress (red) was detected with CellROX and nuclei (blue) were labelled with Hoechst 33342. Shown are the average level of oxidative stress per cell, as the fold change of the untreated control ± SEM for (C) microglial and (D) differentiated neuronal cells. The results are shown from at least 3 independent experiments, with at least 200 cells analyzed per treatment. Scale bars = 10 μm. ***$p < 0.001$.

structural predictions, scaled from 0 to 100. Higher scores indicate higher confidence and better prediction accuracy. A pLDDT above 90 signifies high accuracy for both backbone and side chains, whereas a score above 70 indicates accurate backbone prediction with some side chain errors. The pLDDT score can vary across a protein, indicating regions of differing

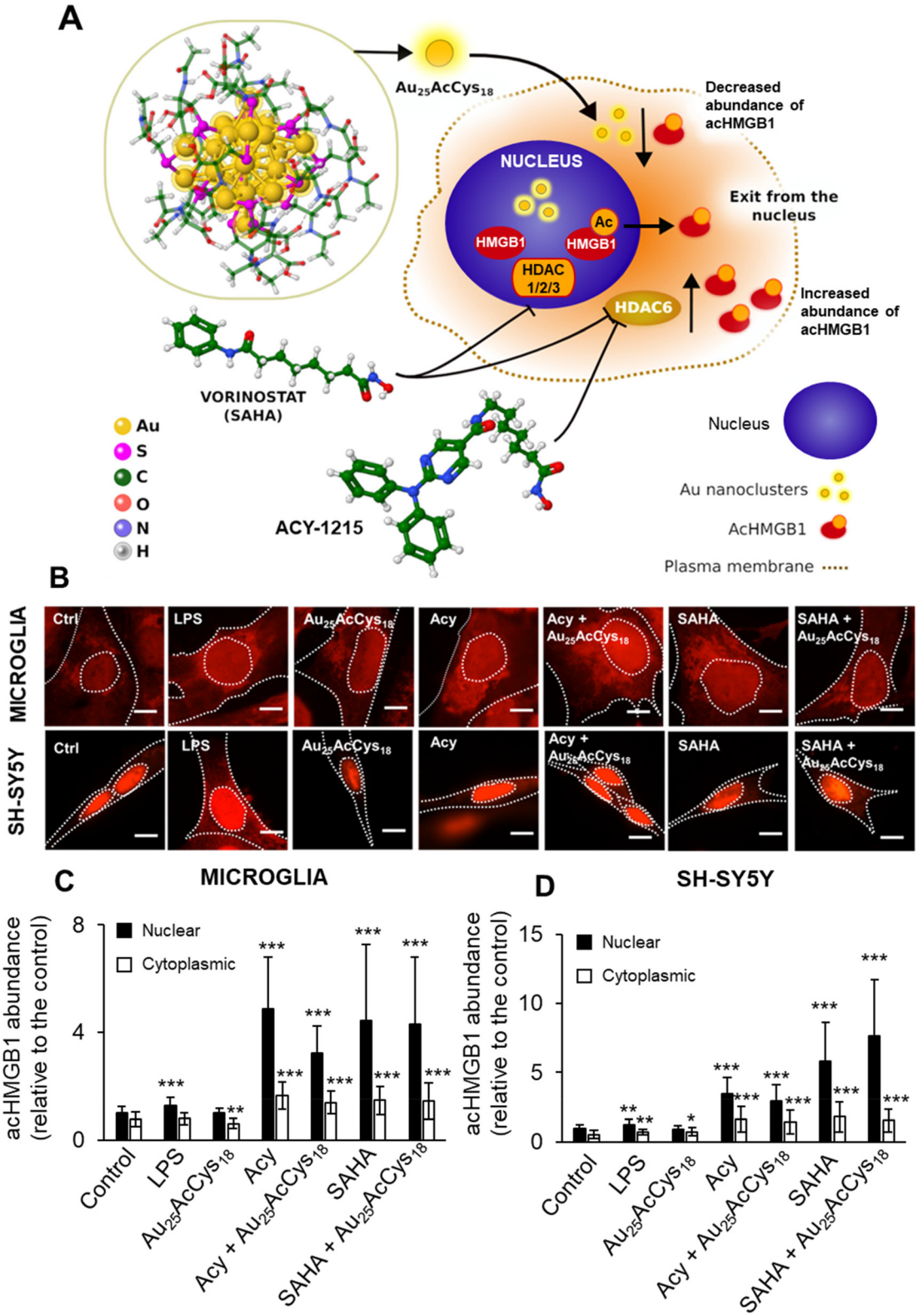

Fig. 4 (A) Schematic of $Au_{25}AcCys_{18}$ as a modulator of acetylated HMGB1 (acHMGB1) and inhibition of histone deacetylases (HDACs) 1, 2, 3, and 6 by vorinostat (SAHA) and ACY-1215. Au = gold, S = sulfur, C = carbon, O = oxygen, N = nitrogen, and H = hydrogen. (B) Fluorescence micrographs of human microglia and differentiated SH-SY5Y neuronal cells treated with lipopolysaccharide (LPS, 10 ng mL^{-1}), $Au_{25}AcCys_{18}$ (1 μM), ACY-1215 (5 μM), and SAHA (5 μM), alone or in combination for 24 h. AcHMGB1 (red) was fluorescently labelled by immunocytochemistry. Nuclei (blue) were labeled with Hoechst 33342. Nuclei and cells are outlined with white dotted lines. Scale bars = 20 μm. Shown are the average level of nuclear and cytoplasmic acHMGB1 per cell ± SEM, in (C) microglial and (D) differentiated neuronal cells, relative to the untreated control (Ctrl), from at least three independent experiments. *$p < 0.05$; **$p < 0.01$; and ***$p < 0.001$.

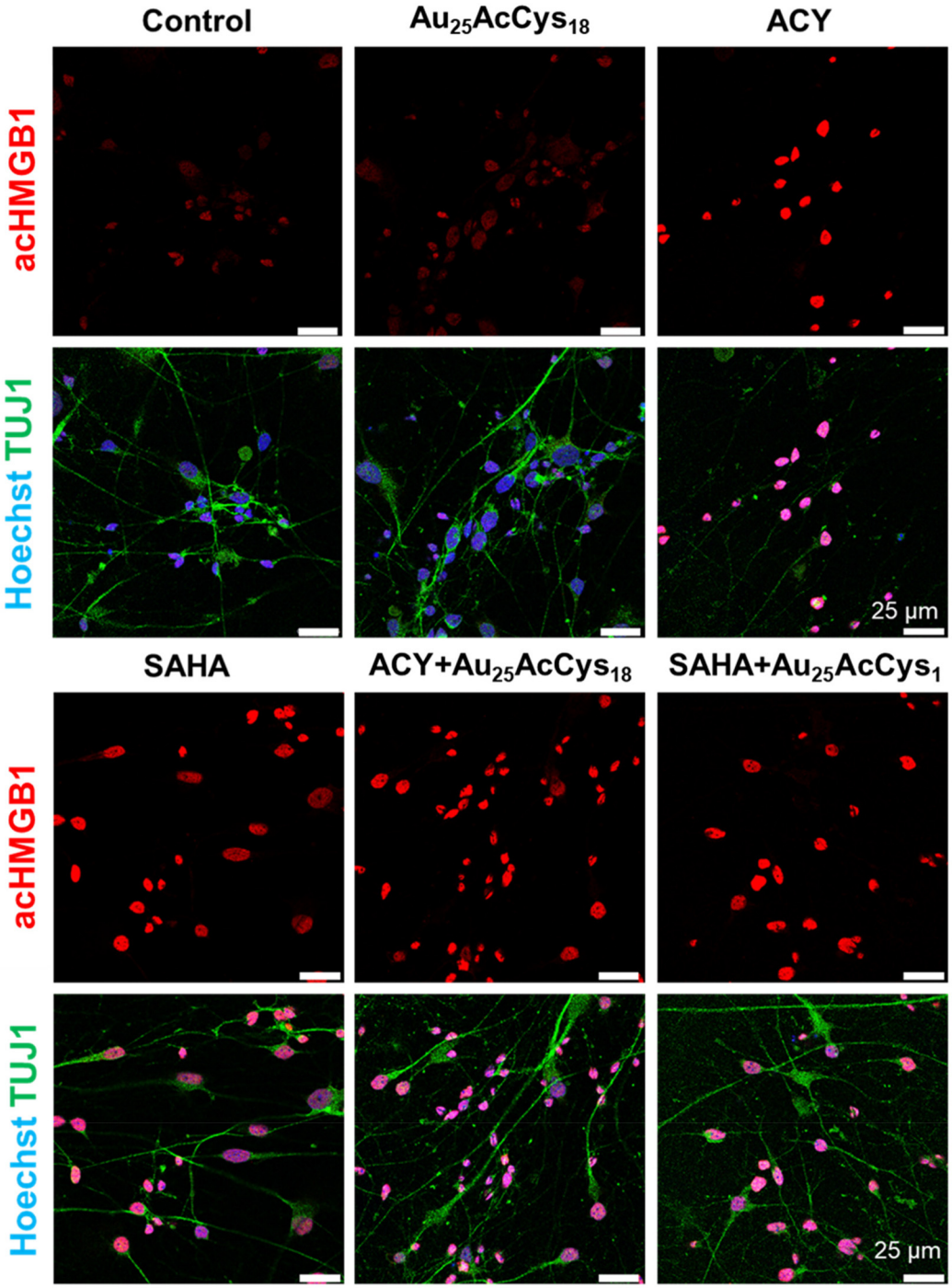

Fig. 5 Representative fluorescence micrographs of acetylated HMGB1 (acHMGB1, red) in human neurons derived from iPSCs treated with $Au_{25}AcCys_{18}$ (1 μM), ACY-1215 (ACY, 5 μM), and vorinostat (SAHA, 5 μM), alone or in combination for 24 h. Neurons were labeled with the neuronal marker TUJ1 (green) and nuclei (blue) were labeled with Hoechst 33342. Cells were fluorescently labeled by immunocytochemistry and imaged using a confocal microscope. Scale bars = 25 μm.

prediction reliability and identifying which parts of the structure are likely accurate. Comparison of the pLDDT plots in Fig. S2a† shows that interacting regions of TFEB and HMGB1 are dark and light blue (pLDDT > 90 and 90 > pLLDT > 70, respectively), indicating high accuracy for the backbone, and slightly less for side chains. On the other hand, the interaction of TFEB and $Au_{25}AcCys_{18}$ was modelled using a sequence of 9 Cys residues due to the need for a flexible model of TFEB, and because only surface ligands of Au_{25}NCs can interact with TFEB. AlphaFold effectively models the flexibility of TFEB and

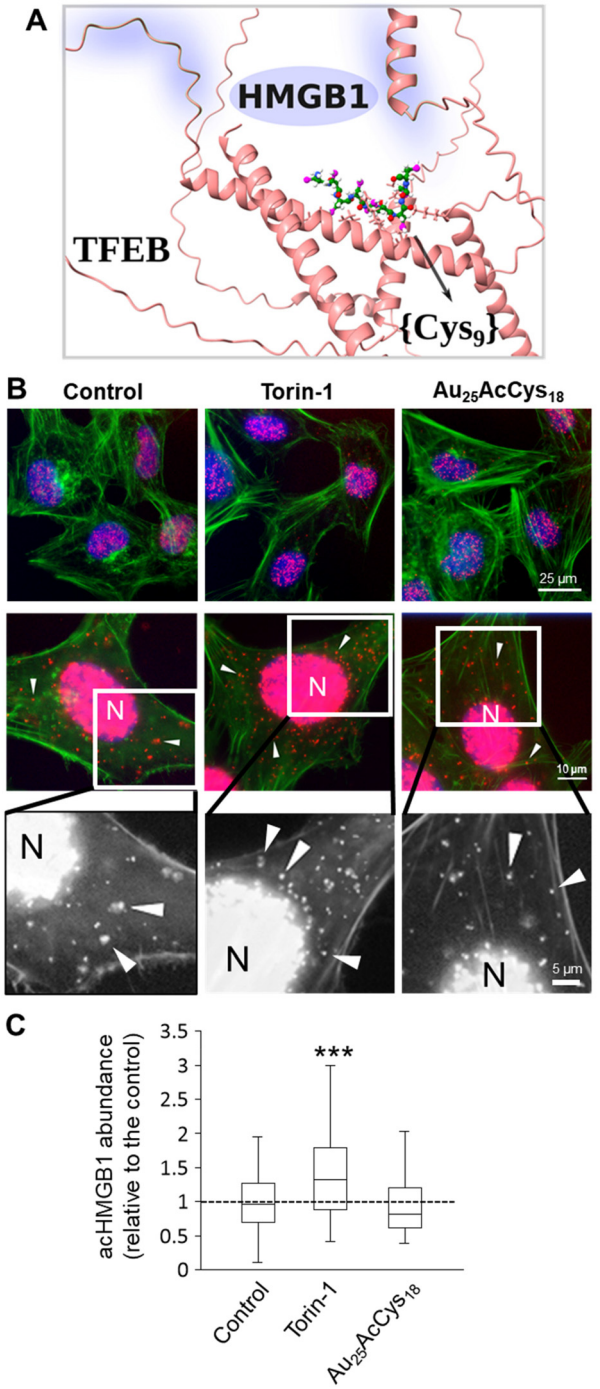

Fig. 6 (A) AlphaFold-modeled structure and interaction between TFEB and {Cys9}, with the position of HMGB1, and TFEB amino acids interacting with HMGB1 highlighted in blue. TFEB (red) is represented by its secondary structures, {Cys9} is represented as balls and sticks (carbon = green, sulfur = magenta, oxygen = red, nitrogen = blue, and hydrogen = white). (B) Fluorescence micrographs at different magnifications (top row at 40X, middle row at 63X, and bottom row as zoomed in panels from 63X) of TFEB–HMGB1 interactions (red, arrows) in human microglia treated with Au25AcCys18 (1 µM, 24 h), as detected by the proximity ligation assay. Torin-1 (250 nM, 24 h) served as a positive control. Nuclei (blue) were labeled with Hoechst 33342, and actin (green) was labeled with Alexa Fluor 488 Phalloidin. (C) Box plots of cytosolic TFEB–HMGB1 interactions per cell, as the fold change of the control (set to 1) from at least 55 cells per condition, and three independent experiments. ***$p < 0.001$.

the $\{Cys_9\}$ ligand, which is crucial for their strong interaction. The model shows the flexibility of TFEB, consistent with its varying NMR structures and shapes $\{Cys_9\}$ for optimal interactions. We also tested a $\{Cys_{18}\}$ model which forms a hairpin and interacts with TFEB similarly to $\{Cys_9\}$. Other docking tools might be less reliable as they use a fixed TFEB structure (which is very flexible in solution), leading to results that heavily depend on the initial TFEB configuration and are unsuitable for large molecules like $Au_{25}AcCys_{18}$. On the other hand, the accuracy of AlphaFold2 can be improved by including the training data and code.[39] Fig. S2b† shows the 3D structure of the TFEB and $\{Cys_9\}$ complex. Comparing the positions of HMGB1 and $\{Cys_9\}$ with TFEB (Fig. 6a), and the interacting amino acids (Fig. S2c and d†) it is apparent that they occupy different parts of TFEB, with different amino acids involved.

The biological association between HMGB1 and TFEB was detected in neural cells using a proximity ligation assay (Fig. 6). Most interactions occur in the nucleus, whereas an increased association in the cytosol is associated with autophagy, as shown in cells treated with the mTOR inhibitor Torin-1 (Fig. 6b and c). $Au_{25}AcCys_{18}$ maintained a level of HMGB1–TFEB association comparable to that of the control condition. An overview of interaction sites between HMGB1 and TFEB is given (Fig. S2a and c†). Additionally, the $\{Cys_9\}$ model for $Au_{25}AcCys_{18}$ and TFEB interaction sites is shown (Fig. S2b and d†).

Discussion

This study addresses the impact and mechanism of atomically defined AuNCs in human neural cells. The rationale for such investigations is a paucity of data for $Au_{25}AcCys_{18}$ in brain cells and a need for a better understanding of intracellular events in human microglia and neurons. So far, $Au_{25}AcCys_{18}$ has not been tested in human neurons derived from iPSCs. This is a close model of human neurons useful for drug and nanostructure screening.[40,41]

It is well established that many stressors, including cerebral hypoxia, lead to hyperactivation of microglia, astrocytes, and deleterious effects in neurons.[42–46] Considering that AuNCs are promising nanotools for imaging and eventual therapeutic intervention, it is a prerequisite to improve our understanding of their deleterious and beneficial effects. Our results show that $Au_{25}AcCys_{18}$ exerts distinct modulatory effects in human microglia, neuron-like cells, and neurons. A decrease in the abundance of ROS under hypoxic and normoxic conditions, maintenance of HMGB1–TFEB association at control levels and low toxicity in human neural cells are novel findings reported herein. Further studies at the level of protein–protein interactions are warranted, particularly in disease models.

Neurological disorders have consistently challenged therapeutic modalities for several reasons; brain accessibility is limited by the size and properties of compounds, and the delicate balance between neural cells does not accommodate drastic manipulations without significant side effects and

sequelae. Yet, the demand for better diagnostic solutions and brain drugs continues to grow globally. Nanotechnological approaches to the brain offer several advantages. AuNCs in this study are atomically defined and can be as small as a few nanometers, with tunable surface properties. These features can facilitate blood–brain barrier entry and discourage unwanted immune reactivity. Microglia are often the first responders in the brain; by consuming and interacting with AuNCs, they can directly or indirectly influence other neural cells.[3,4,47,48] AuNCs seem to have a range of effects relevant to neurological disorders, particularly when functionalized with AcCys, which is key to antioxidant defenses. By altering ROS levels, $Au_{25}AcCys_{18}$ modulates hypoxia-driven pathways, which would otherwise exacerbate microenvironmental damage in brain cancer and stroke.[49–51] Microglial hyperactivation is also a source of excessive ROS, and when unopposed due to ineffective endogenous antioxidant molecules or enzymatic function, it results in impaired cellular functions. Our studies show remarkable effects of $Au_{25}AcCys_{18}$ in normalizing ROS concentrations under normoxic and hypoxic conditions.

We investigated if the AuNCs could have subtle effects on protein–protein interactions, particularly with redox-responsive transcription factors TFEB and HMGB1. The AuNC interactome is only beginning to be studied. Interaction partners can be partially surmised based on subcellular localization. We investigated lysosomal proteins because HMGB1 is trafficked through lysosomal compartments upon its acetylation and extranuclear release.[52,53] Its alarmin function is enhanced by pro-inflammagens, making it a pharmacological target.[20,54] Although $Au_{25}AcCys_{18}$ does not directly affect HMGB1 acetylation (*e.g.* by modulating acetylases or deacetylases), it attenuates the effect of deacetylase inhibitors in neuron-like cells. This might indicate that $Au_{25}AcCys_{18}$ exerts mainly cytosolic effects, as pan- (vorinostat, SAHA) and cytosolic (ACY-1215) histone deacetylase inhibitors had similar results. In addition, ROS can increase extranuclear HMGB1 and TFEB activation through the lysosomal sensor TRPML1.[55] Thus, AuNC-mediated normalization of ROS could also normalize HMGB1 localization and benefit inflammatory resolution.

TFEB participates in the regulation of lysosomal function and biogenesis as well as cellular adaptation under stress.[56] Effects of $Au_{25}AcCys_{18}$ on lysosomes were investigated through TFEB activation, cathepsin activity, and TFEB interactions. TFEB–HMGB1 interactions detected by the proximity ligation assay indicate that most interactions are nuclear, as both proteins are transcription regulators abundant in the nucleus.[37,57,58] Cytosolic interactions increased upon mTOR inhibition with Torin-1, indicating that TFEB and HMGB1 interaction could participate in autophagy.[59] TFEB and HMGB1 coincide in their interaction with autophagic flux regulator Beclin-1, thus contributing to the same protein complexes and pathways.[60,61] TFEB acetylation at several lysine residues is also a determinant of its dimerization and transcriptional activity, sometimes with opposing effects.[37,62] TFEB and HMGB1 can undergo several types of post-translational modifications (PTMs), including phosphorylation and oxidation.[37,52,62,63] Such modifications under oxidative stress could alter their interaction affinity for other redox-responsive proteins, and variable adaptability could make neurons particularly vulnerable. Under oxidative stress, TFEB can be oxidized and prone to dimerization. AcHMGB1 has a limited ability to interact with AuNCs,[4] suggesting that PTMs contribute to altered protein–protein interactions. It remains to be examined how phosphorylated HMGB1 and TFEB differ in their interaction, and how other PTMs influence their interaction in models of neurological disorders.

The models of TFEB–HMGB1 and TFEB–$Au_{25}AcCys_{18}$ interactions were studied using AlphaFold as implemented in Chimerax. Thus, the flexibility of all interacting partners was considered. The results clearly show that critical sites for the TFEB–HMGB1 interaction are TFEB residues Y75 to Q86 and S209 to K219, whereas a distinct set of TFEB residues (K237 to K274) is involved in interactions with the $\{Cys_9\}$ model of $Au_{25}AcCys_{18}$. Interactions involve both charged and hydrophobic amino acids, which form ion–ion and hydrophobic connections between TFEB and HMGB1, or the $\{Cys_9\}$ model. Advantages of AlphaFold2 predictions include the possibility to accurately model multiunit protein–protein complexes from their primary sequences without the need for resolved crystal structures, whereas the pLDDT metric offers a quantitative assessment of the models. As only the protein parts of the Protein Data Bank structures were used as the AlphaFold2 training set, this method cannot model small molecules, DNA or post-translational modifications, and it struggles to predict the impact of point mutations.

In summary, results from our studies suggest that $Au_{25}AcCys_{18}$ (i) is only toxic at high concentrations in human neurons and glia; (ii) reduces oxidative stress under hypoxic and normoxic conditions and (iii) maintains HMGB1–TFEB association in human neural cells at the control level. These novel findings provide a first step in future connectome investigations in human neural cells exposed to or treated with AuNCs. They also point towards studies on how AuNCs could affect other transcription factor complexes under physiological and pathological conditions in cell models, particularly human organoids.

Conclusions

The motivation for this study stems from seminal discoveries highlighting the unique properties of AuNCs using several complementary experimental techniques and computational methods.[3,64,65] $Au_{25}AcCys_{18}$ is particularly interesting because it does not seem harmful to human cells within the concentration range and models proposed. They were tested for bioimaging,[15,66–68] and our recent studies explain the uniqueness of Au_{25} with 16 ligands, supporting the notion that this type of nanocluster is a "captain of the big ship".[69] We provide new insight into some biological effects in neural cells and show that $Au_{25}AcCys_{18}$ could interact with the transcription

factor TFEB (computational model), modulate HMGB1 localization without markedly increasing its abundance, and normalize excessive levels of ROS under hypoxic and normoxic conditions. Considering that so far $Au_{25}AcCys_{18}$ has not been tested in human neurons derived from iPSCs, we aim to stimulate further preclinical investigations on AuNCs in human brain models (*e.g.* organoids). As our studies are limited to HMGB1–TFEB association in the presence of $Au_{25}AcCys_{18}$, this is a first step in future connectome investigations in human neural cells exposed to or treated with AuNCs. Further investigations on the likely modulatory effects of different protein–protein associations are warranted.

Author contributions

DM, IZ, and ZSM conceptualized the studies and wrote the manuscript drafts and revisions. IZ and MB performed all experiments in cells, and ZQY performed experiments in iPSC-derived neurons. PD and GR supervised experiments in iPSC-derived neurons. ZSM, AM, and MPB carried out modeling, analyzed and prepared the results in publishable format. VBK and AR participated in the initial experimental plan and provided feedback on the text.

Data availability

The data supporting this article have been included as part of the ESI.†

Conflicts of interest

There are no conflicts of interest to declare.

Acknowledgements

DM acknowledges funding from FRQ-S (#294233) and NSERC (RGPIN 2020-07011). ZSM and VBK were supported by the project STIM-REI (contract number: KK.01.1.1.01.0003), funded by the European Union through the European Regional Development Fund—the Operational Programme Competitiveness and Cohesion 2014-2020 (KK.01.1.1.01). GR is funded by the ALS-Canada-Brain Canada Arthur J. Hudson Translation Team Grant. VBK, ZSM, MPB and AM acknowledge funding from "Confined molecular systems: from a new generation of materials to the stars" (COSY) supported by COST (European Cooperation in Science and Technology).

References

1 V. Bonačić-Koutecký and R. Antoine, *Nanoscale*, 2019, **11**, 12436–12448.
2 S. M. van de Looij, E. R. Hebels, M. Viola, M. Hembury, S. Oliveira and T. Vermonden, *Bioconjugate Chem.*, 2022, **33**, 4–23.
3 H. Fakhouri, M. P. Bakulić, I. Zhang, H. Yuan, D. Bain, F. Rondepierre, P.-F. Brevet, Ž. S. Maršić, R. Antoine, V. Bonačić-Koutecký and D. Maysinger, *Commun. Chem.*, 2023, **6**, 1–10.
4 D. Maysinger, Ž. Sanader Maršić, E. R. Gran, A. Shobo, J.-R. Macairan, I. Zhang, M. Perić Bakulić, R. Antoine, G. Multhaup and V. Bonačić-Koutecký, *ACS Chem. Neurosci.*, 2022, **13**, 464–476.
5 Y. Negishi, K. Nobusada and T. Tsukuda, *J. Am. Chem. Soc.*, 2005, **127**, 5261–5270.
6 L. Zhu, Y. Zeng, M. Teubner, B. Grimm-Lebsanft, A. R. Ziefuß, C. Rehbock, M. A. Rübhausen, S. Barcikowski, W. J. Parak and I. Chakraborty, *ACS Appl. Nano Mater.*, 2021, **4**, 3197–3203.
7 S. R. Bhattacharya, K. Bhattacharya, V. J. Xavier, A. Ziarati, D. Picard and T. Bürgi, *ACS Appl. Mater. Interfaces*, 2022, **14**, 29521–29536.
8 S. Tian, Y. Cao, T. Chen, S. Zang and J. Xie, *Chem. Commun.*, 2020, **56**, 1163–1174.
9 G. F. Combes, A.-M. Vučković, M. Perić Bakulić, R. Antoine, V. Bonačić-Koutecky and K. Trajković, *Cancers*, 2021, **13**, 4206.
10 H. Huang, R. Liu, J. Yang, J. Dai, S. Fan, J. Pi, Y. Wei and X. Guo, *Pharmaceutics*, 2023, **15**, 1868.
11 J. Yang, F. Yang, C. Zhang, X. He and R. Jin, *ACS Mater. Lett.*, 2022, **4**, 1279–1296.
12 J. Peng and X. Liang, *Medicine*, 2019, **98**, e15311.
13 A.-M. Hada, A.-M. Craciun, M. Focsan, A. Vulpoi, E.-L. Borcan and S. Astilean, *Microchim. Acta*, 2022, **189**, 337.
14 M. Hembury, N. Beztsinna, H. Asadi, J. B. van den Dikkenberg, J. D. Meeldijk, W. E. Hennink and T. Vermonden, *Biomacromolecules*, 2018, **19**, 2841–2848.
15 C. Zhang, X. Gao, W. Chen, M. He, Y. Yu, G. Gao and T. Sun, *iScience*, 2022, **25**, 105022.
16 X. Yuan, Y. Yu, Q. Yao, Q. Zhang and J. Xie, *J. Phys. Chem. Lett.*, 2012, **3**, 2310–2314.
17 L.-P. Bernier, E. M. York and B. A. MacVicar, *Trends Neurosci.*, 2020, **43**, 854–869.
18 T. F. Outeiro, P. S. Brocardo and D. P. Gelain, *J. Neurochem.*, 2024, **168**, 1423–1425.
19 C. Pallarés-Moratalla and G. Bergers, *Front. Immunol.*, 2024, **15**, 1305087.
20 U. Andersson, H. Yang and H. Harris, *Expert Opin. Ther. Targets*, 2018, **22**, 263–277.
21 U. Andersson and H. Yang, *J. Intensive Care Med.*, DOI: **10.1016/j.jointm.2022.02.001**.
22 H. M. Berman, J. Westbrook, Z. Feng, G. Gilliland, T. N. Bhat, H. Weissig, I. N. Shindyalov and P. E. Bourne, *Nucleic Acids Res.*, 2000, **28**, 235–242.
23 J. Jumper, R. Evans, A. Pritzel, T. Green, M. Figurnov, O. Ronneberger, K. Tunyasuvunakool, R. Bates, A. Žídek, A. Potapenko, A. Bridgland, C. Meyer, S. A. A. Kohl,

A. J. Ballard, A. Cowie, B. Romera-Paredes, S. Nikolov, R. Jain, J. Adler, T. Back, S. Petersen, D. Reiman, E. Clancy, M. Zielinski, M. Steinegger, M. Pacholska, T. Berghammer, S. Bodenstein, D. Silver, O. Vinyals, A. W. Senior, K. Kavukcuoglu, P. Kohli and D. Hassabis, *Nature*, 2021, **596**, 583–589.

24 M. Mirdita, K. Schütze, Y. Moriwaki, L. Heo, S. Ovchinnikov and M. Steinegger, *Nat. Methods*, 2022, **19**, 679–682.

25 Jmol: an open-source Java viewer for chemical structures in 3D. **https://www.jmol.org/**.

26 E. C. Meng, T. D. Goddard, E. F. Pettersen, G. S. Couch, Z. J. Pearson, J. H. Morris and T. E. Ferrin, *Protein Sci.*, 2023, **32**, e4792.

27 J. P. Perdew, J. A. Chevary, S. H. Vosko, K. A. Jackson, M. R. Pederson, D. J. Singh and C. Fiolhais, *Phys. Rev. B: Condens. Matter Mater. Phys.*, 1992, **46**, 6671–6687.

28 J. P. Perdew, M. Ernzerhof and K. Burke, *J. Chem. Phys.*, 1996, **105**, 9982–9985.

29 F. Weigend and R. Ahlrichs, *Phys. Chem. Chem. Phys.*, 2005, **7**, 3297–3305.

30 J. S. Binkley, J. A. Pople and W. J. Hehre, *J. Am. Chem. Soc.*, 1980, **102**, 939–947.

31 K. D. Dobbs and W. J. Hehre, *J. Comput. Chem.*, 1987, **8**, 880–893.

32 M. Dolg, H. Stoll and H. Preuss, *J. Chem. Phys.*, 1989, **90**, 1730–1734.

33 S. Stern, R. Santos, M. C. Marchetto, A. P. D. Mendes, G. A. Rouleau, S. Biesmans, Q.-W. Wang, J. Yao, P. Charnay, A. G. Bang, M. Alda and F. H. Gage, *Mol. Psychiatry*, 2018, **23**, 1453–1465.

34 M. W. Heaven, A. Dass, P. S. White, K. M. Holt and R. W. Murray, *J. Am. Chem. Soc.*, 2008, **130**, 3754–3755.

35 M. Zhu, C. M. Aikens, F. J. Hollander, G. C. Schatz and R. Jin, *J. Am. Chem. Soc.*, 2008, **130**, 5883–5885.

36 B. Pedre, U. Barayeu, D. Ezeriņa and T. P. Dick, *Pharmacol. Ther.*, 2021, **228**, 107916.

37 H. Chen, S. Gong, H. Zhang, Y. Chen, Y. Liu, J. Hao, H. Liu and X. Li, *Cell Death Discovery*, 2024, **10**, 84.

38 R. Yin, B. Y. Feng, A. Varshney and B. G. Pierce, *Protein Sci.*, 2022, **31**, e4379.

39 G. Ahdritz, N. Bouatta, C. Floristean, S. Kadyan, Q. Xia, W. Gerecke, T. J. O'Donnell, D. Berenberg, I. Fisk, N. Zanichelli, B. Zhang, A. Nowaczynski, B. Wang, M. M. Stepniewska-Dziubinska, S. Zhang, A. Ojewole, M. E. Guney, S. Biderman, A. M. Watkins, S. Ra, P. R. Lorenzo, L. Nivon, B. Weitzner, Y.-E. A. Ban, S. Chen, M. Zhang, C. Li, S. L. Song, Y. He, P. K. Sorger, E. Mostaque, Z. Zhang, R. Bonneau and M. AlQuraishi, *Nat. Methods*, 2024, **21**, 1514–1524.

40 R. Dolmetsch and D. H. Geschwind, *Cell*, 2011, **145**, 831–834.

41 K. Takahashi, K. Tanabe, M. Ohnuki, M. Narita, T. Ichisaka, K. Tomoda and S. Yamanaka, *Cell*, 2007, **131**, 861–872.

42 P.-B. Bielawski, I. Zhang, C. Correa-Paz, F. Campos, M. Migliavacca, E. Polo, P. Del Pino, B. Pelaz, D. Vivien and D. Maysinger, *ACS Pharmacol. Transl. Sci.*, 2024, **7**, 680–692.

43 S. Y. Lee and W.-S. Chung, *Curr. Opin. Neurobiol.*, 2024, **84**, 102840.

44 S. A. Liddelow, K. A. Guttenplan, L. E. Clarke, F. C. Bennett, C. J. Bohlen, L. Schirmer, M. L. Bennett, A. E. Münch, W.-S. Chung, T. C. Peterson, D. K. Wilton, A. Frouin, B. A. Napier, N. Panicker, M. Kumar, M. S. Buckwalter, D. H. Rowitch, V. L. Dawson, T. M. Dawson, B. Stevens and B. A. Barres, *Nature*, 2017, **541**, 481–487.

45 W. Lu and J. Wen, *Mol. Neurobiol.*, 2024, **61**, 6161–6174.

46 G. Nzou, R. T. Wicks, N. R. VanOstrand, G. A. Mekky, S. A. Seale, A. El-Taibany, E. E. Wicks, C. M. Nechtman, E. J. Marrotte, V. S. Makani, S. V. Murphy, M. C. Seeds, J. D. Jackson and A. J. Atala, *Sci. Rep.*, 2020, **10**, 9766.

47 C. C. Escoubas and A. V. Molofsky, *Trends Immunol.*, 2024, **45**, 358–370.

48 S. Zhao, A. D. Umpierre and L.-J. Wu, *Trends Neurosci.*, 2024, **47**, 181–194.

49 N. Colwell, M. Larion, A. J. Giles, A. N. Seldomridge, S. Sizdahkhani, M. R. Gilbert and D. M. Park, *Neuro-Oncology*, 2017, **19**, 887–896.

50 N. Lénárt, C. Cserép, E. Császár, B. Pósfai and Á. Dénes, *Glia*, 2024, **72**, 833–856.

51 A. M. Planas, *Glia*, 2024, **72**, 1016–1053.

52 U. Andersson, D. J. Antoine and K. J. Tracey, *J. Intern. Med.*, 2014, **276**, 420–424.

53 R. Chen, R. Kang and D. Tang, *Exp. Mol. Med.*, 2022, **54**, 91–102.

54 M. E. Street, *Horm. Res. Paediatr.*, 2020, **93**, 73–75.

55 X. Zhang, X. Cheng, L. Yu, J. Yang, R. Calvo, S. Patnaik, X. Hu, Q. Gao, M. Yang, M. Lawas, M. Delling, J. Marugan, M. Ferrer and H. Xu, *Nat. Commun.*, 2016, **7**, 12109.

56 N. Raben and R. Puertollano, *Annu. Rev. Cell Dev. Biol.*, 2016, **32**, 255–278.

57 Y. Feng, Y. Chen, X. Wu, J. Chen, Q. Zhou, B. Liu, L. Zhang and C. Yi, *Autophagy*, 2024, **20**, 4–14.

58 M. T. Lotze and K. J. Tracey, *Nat. Rev. Immunol.*, 2005, **5**, 331–342.

59 D. Tang, R. Kang, K. M. Livesey, C.-W. Cheh, A. Farkas, P. Loughran, G. Hoppe, M. E. Bianchi, K. J. Tracey, H. J. Zeh and M. T. Lotze, *J. Cell Biol.*, 2010, **190**, 881–892.

60 X. Ma, H. Liu, J. T. Murphy, S. R. Foyil, R. J. Godar, H. Abuirqeba, C. J. Weinheimer, P. M. Barger and A. Diwan, *Mol. Cell. Biol.*, 2015, **35**, 956–976.

61 M. Palmieri, S. Impey, H. Kang, A. di Ronza, C. Pelz, M. Sardiello and A. Ballabio, *Hum. Mol. Genet.*, 2011, **20**, 3852–3866.

62 J. A. Martina, D. Guerrero-Gómez, E. Gómez-Orte, J. Antonio Bárcena, J. Cabello, A. Miranda-Vizuete and R. Puertollano, *EMBO J.*, 2021, **40**, e105793.

63 M. Takla, S. Keshri and D. C. Rubinsztein, *EMBO Rep.*, 2023, **24**, e57574.

64 M. Perić, Ž. S. Maršić, I. Russier-Antoine, H. Fakhouri, F. Bertorelle, P.-F. Brevet, X. le Guével, R. Antoine and

V. Bonačić-Koutecký, *Phys. Chem. Chem. Phys.*, 2019, **21**, 23916–23921.
65 H. Qian, M. Zhu, Z. Wu and R. Jin, *Acc. Chem. Res.*, 2012, **45**, 1470–1479.
66 J. Ma, M. Yang, B. Zhang and M. Niu, *Nanoscale*, 2024, **16**, 7287–7306.
67 K. Tan, H. Ma, X. Mu, Z. Wang, Q. Wang, H. Wang and X.-D. Zhang, *Anal. Bioanal. Chem.*, 2024, **416**, 5871–5891.
68 H. Yang, Y. Wu, H. Ruan, F. Guo, Y. Liang, G. Qin, X. Liu, Z. Zhang, J. Yuan and X. Fang, *Anal. Chem.*, 2022, **94**, 3056–3064.
69 X. Kang, H. Chong and M. Zhu, *Nanoscale*, 2018, **10**, 10758–10834.